

Eruption Forecasting of Strokkur Geyser, Iceland, Using Permutation Entropy

Maria R.P. Sudibyo¹, Eva P.S. Eibl¹, Sebastian Hainzl², Gylfi Páll Hersir^{3,4}

¹University of Potsdam, Institute for Geosciences, Karl-Liebknecht-Str.24/25, Potsdam-Golm

²GFZ German Research Centre for Geosciences, Telegrafenberg, 14473 Potsdam, Germany

³ISOR, Iceland GeoSurvey, Urdarhvarf 8, Reykjavik, Iceland

⁴Presently gylfi.pall@outlook.com

Key Points:

- Permutation Entropy (PE) is a simple tool to assess the complexity of a time series.
- We analyzed the PE evolution for 63 eruptive cycles of Strokkur geyser and found characteristic changes in PE during recharge.
- PE is found to be a useful statistical predictor of the eruption times and highlights the precursor 15 s before eruptions.

Corresponding author: Maria R.P. Sudibyo, pujastutisudibyo@uni-potsdam.de

Abstract

A volcanic eruption is usually preceded by seismic precursors, but their interpretation and use for forecasting the eruption onset time remain a challenge. Eruption processes in geysers are similar to volcanoes, but occur more frequently. Therefore, geysers are useful sites for testing new forecasting methods. We tested the application of Permutation Entropy (PE) as a robust method to assess the complexity in seismic recordings of the Strokkur geyser, Iceland. Strokkur features several minute-long eruptive cycles, enabling us to verify in 63 recorded cycles whether PE behaves consistently from one eruption to the next one. We performed synthetic tests to understand the effect of different parameter settings in the PE calculation. Our application to Strokkur shows a distinct, repeating PE pattern consistent with previously identified phases in the eruptive cycle. We find a systematic increase in PE within the last 15 s before the eruption, indicating that an eruption will occur. We quantified the predictive power of PE, showing that PE performs better than seismic signal strength or quiescence when it comes to forecasting eruptions.

Plain Language Summary

When a volcano shows the first sign of activity, it is challenging to determine whether and when the actual eruption will occur. Usually, researchers create earthquake lists and locate these events to assess this. However, an alternative and simpler method can be directly applied to continuous seismic data. We tested a method that assesses the complexity of signals. We first created synthetic data to find reasonable parameter settings for this method. While volcanoes do not erupt very often, frequent eruptions at geysers allow us to systematically study and compare several eruptions. We analyzed the continuous record of 63 eruptions of the Strokkur geyser, Iceland. Our results show a distinct pattern that repeats from one eruption to the next one. We also find a clear pattern that indicates about 15 s before the next eruption that an eruption will occur. We show that this method performs better in eruption forecasting than assessing the seismic noise or silence caused by the geyser.

1 Introduction

When a volcano becomes restless, it is challenging to assess whether it will lead to an actual eruption and determine the timing of the eruption onset. A magmatic intrusion starting at depth can (i) remain at depth, (ii) stall just before reaching the surface, (iii) erupt in sluggish and viscous extrusion, or (iv) erupt rapidly or explosively (Moran et al., 2011). The process of magma migration involves interactions with the surrounding country rock, cooling magma bodies from previous eruptions, and (or) hydrothermal system (Moran et al., 2008). These interactions generate natural phenomena such as earthquakes, deformation, temperature changes, and gas emissions. These phenomena can be observed by geophysical and geochemical measurements (Moran et al., 2008) and integrated with the history of past eruptions in a framework of eruption forecasting (Whitehead & Bebbington, 2021).

From a seismic point of view, eruptions can show precursors such as accelerating or decelerating earthquake rates. To assess this, monitoring institutes conventionally use methods to tabulate daily event counts (McNutt, 1996) and calculate the average amplitude for a certain window length (Endo & Murray, 1991). The Failure Forecast Method estimates the onset time of eruption by using the rate and the acceleration of seismic precursors associated with the rock failure caused by magma propagation (Boué et al., 2015). However, this method cannot deal with complex precursory signals, e.g., that exhibits fluctuations or deceleration (Boué et al., 2015). Furthermore, due to the uncertainty of the eruption forecast and numerous false alarms (Bell et al., 2013), this method is not recommended to be stand-alone (Whitehead & Bebbington, 2021). Dempsey et al. (2020) tested a real-time Machine Learning framework to detect eruption precursors of five ma-

65 jor eruptions at Whakaari volcano, New Zealand, from 2011 to 2020. This framework
 66 derives the information from the seismic amplitude between different frequency bands
 67 to assess whether an eruption will occur. A challenge lies in the threshold determina-
 68 tion: while increasing the threshold will eliminate false predictions, it leads to missing
 69 eruptions and vice versa.

70 A robust forecasting framework requires incorporating different forecasting attributes
 71 from multiple methods. Developing or testing the application of new methods is impor-
 72 tant to improve the reliability of the forecasting framework. Permutation Entropy, here-
 73 inafter referred to as PE, has been proposed to be a promising tool for eruption forecast-
 74 ing (Glynn & Konstantinou, 2016), but the limitation of this method is currently not
 75 yet well-defined. PE quantifies the complexity of time series in a simple way, allowing
 76 us to characterize the evolution of a dynamic system (Bandt & Pompe, 2002; Zanin et
 77 al., 2012; Riedl et al., 2013).

78 Geysers are hot springs characterized by intermittent discharge of water that erupts
 79 turbulently and is accompanied by a vapor phase (White, 1967). The eruption process
 80 of geysers requires magmatism as a heat source, abundant water recharge, and a plumb-
 81 ing system (Hurwitz & Manga, 2017). While the type of liquid and gas phase in geysers
 82 differs from the liquid, gas, and solid phase in magma, the fluid is driven to eruption by
 83 the gases in both cases. Therefore, the knowledge gained from understanding geyser erup-
 84 tions might provide useful insights for monitoring volcanic eruptions.

85 Here, we tested the application of PE for forecasting eruptions at Strokkur geyser,
 86 Iceland (Fig. 1a and b). The Strokkur geyser is an ideal site for three reasons: (1) Strokkur
 87 features a several-minute long eruptive cycle (Eibl et al., 2021) which allows us to check
 88 if PE behaves consistently from one cycle to the next one, (2) the features of the erup-
 89 tive cycle were already described and interpreted multidisciplinary (Eibl et al., 2021) and
 90 provide a benchmark for our study, (3) the available instrument network (Fig. 1b) con-
 91 sists of seismometers located at a few meter distance from the geyser’s conduit, provid-
 92 ing signals with a high signal-to-noise ratio, and seismometers installed at 40 to 50 m dis-
 93 tance, providing a good configuration to test the sensitivity of PE towards station dis-
 94 tance.

95 In this publication, we firstly introduce the PE method (section 2.1) and perform
 96 several synthetic tests to choose the optimum parameters for PE calculations (section 2.2).
 97 We also introduce the Receiver Operating Characteristic (ROC) analysis (section 2.3)
 98 to assess the predictive power of PE. Then, the methods are applied to eruptions of the
 99 Strokkur geyser (section 3 and 4). We compare PE with seismic root-mean-square val-
 100 ues (RMS) for one eruptive cycle (section 5.1) and stacked for all available single erup-
 101 tive cycles (section 5.2). We assess PE for other eruption types (section 5.3) and the de-
 102 pendence of PE on distance (section 5.4). We discuss how PE relates to the seismic sources
 103 migration (section 6.1) and its predictive power for eruptions at the Strokkur geyser (sec-
 104 tion 6.3). We conclude that PE detects a clear precursory signal at stations at a few met-
 105 er distance, making it a promising tool in eruption forecasting.

106 2 Methods and Synthetic Test

107 2.1 Calculation of Permutation Entropy (PE)

108 Permutation Entropy is a robust way to quantify the complexity of a time series
 109 (Bandt & Pompe, 2002; Zanin et al., 2012; Riedl et al., 2013). This PE method analyzes
 110 the probability distribution of ordinal patterns observed in the data (Bandt & Pompe,
 111 2002). An ordinal pattern is a vector representing the relative order of amplitude of the
 112 successive samples in a sequence of time series (Bandt & Pompe, 2002; Zanin et al., 2012;
 113 Riedl et al., 2013). For example, a sequence of {0.5, 1.0, 3.5, 4.0, 5.7}, based on their

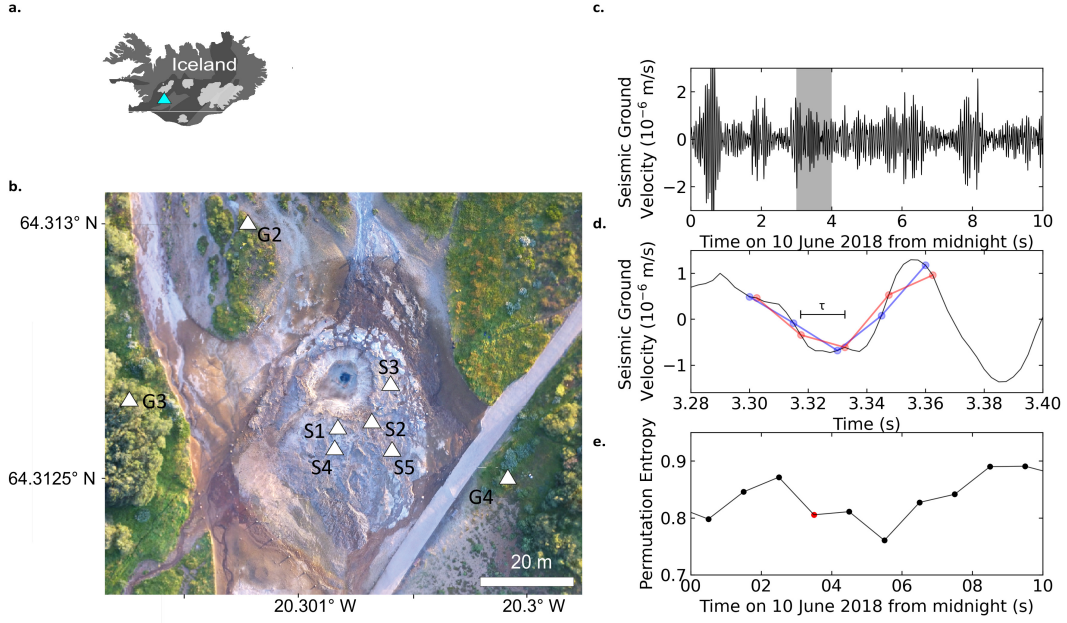


Figure 1. Overview of station network near Strokkur geyser, Iceland and the calculation of PE. (a) Location of the Strokkur geyser in Iceland (blue triangle) and (b) aerial map where white triangles indicate the location of the seismometers (7L network). (c) 10 s seismogram recorded by the vertical component of station S1. The seismogram is divided into 10 bins of 1 s. The shaded part is related to one of those bins. (d) A closer view of 0.12 s seismic data taken from the shaded window in subfigure (c). The blue and red dot-connecting-lines visualize two consecutive ordinal patterns, $\{3, 1, 0, 2, 4\}$ and $\{2, 1, 0, 3, 4\}$ respectively. Each pattern is constructed from five consecutive values selected using $m = 5$ and $\tau = 0.0015$ s. The length of τ is visualized as a black horizontal scalebar. (e) The 10 PE values calculated for the consecutive 1 s time window in subfigure (c), where the red dot refers to the PE calculated for the shaded time window in subfigure (c).

114
115

amplitude order, is represented as an ordinal pattern of $\{0, 1, 2, 3, 4\}$ and a sequence of $\{1.1, 0.8, 0.7, 1.3, 1.0\}$ is represented as an ordinal pattern of $\{3, 1, 0, 4, 2\}$.

116
117
118
119
120
121
122
123
124
125

To construct an ordinal pattern, we basically downsample the time series using an embedding dimension and a delay time. The embedding dimension is the number of samples used to construct an ordinal pattern, i.e., the length of the ordinal pattern, while the delay time is the time gap between the successive samples constructing the ordinal pattern. The ordinal pattern is then defined by a vector of $x_s, x_{s+\tau}, \dots, x_{s+(m-1)\tau}$, where x_s is the first sample in the sequence, m is the embedding dimension and τ is the delay time (Zanin et al., 2012; Riedl et al., 2013). If equal values of amplitude are selected, these values are ranked based on their temporal order (Zunino et al., 2017). To extract all ordinal patterns in a short time window, we continuously shift x_s one sample forward until the last ordinal pattern reaches the end of the window. The PE for the time bin

126 is then calculated as follows:

$$PE = \frac{-1}{\log_2 m!} \sum_{k=1}^{m!} p_k \log_2 p_k \quad (1)$$

127 where p_k is the probability of the ordinal pattern k , and m is the value of the embed-
 128 ding dimension. p_k is estimated by the relative frequency N_k/N , where N_k represents
 129 the number of recurrences of pattern k and N is the total number of ordinal patterns
 130 observed in the time window. The maximum number of different ordinal patterns in a
 131 time series signal is $m!$. Equation (1) is normalized with $\log_2(m!)$ to limit the value of
 132 PE to the range of 0 to 1. We then repeat the PE calculation for the next time bin that
 133 does not overlap with the previous one until the whole time period of interest is processed,
 134 and we can study the PE changes in time.

135 An example of PE calculated for seismic data of station S1 at Strokkur (see Fig. 1b)
 136 is illustrated in Fig. 1c-e. Here, we first divided the seismic time series into 1 s-windows
 137 (Fig. 1c), in which the ordinal patterns were extracted using $m = 5$ and $\tau = 0.015$ s
 138 (Fig. 1d). We define the delay time as the time gap in seconds as we deal with seismic
 139 time series that were recorded with different sampling rates. In each 1 s-window, we then
 140 estimated the probability distribution of the ordinal patterns and calculated the respec-
 141 tive PE value (Fig. 1e).

142 2.2 Synthetic Test of Permutation Entropy

143 The calculation of PE requires the choice of the delay time, embedding dimension,
 144 and the length of time bins (e.g., the shaded window in Fig. 1c). We created several syn-
 145 thetic signals with and without noise to explore the role of these parameters and to de-
 146 fine reasonable settings for the PE calculation. The synthetic signals were generated us-
 147 ing the basic formula $x(t) = \sin(2\pi ft)$ and a sampling rate of 100 Hz. We set the length
 148 of the signals to 20000 s. For all tests, we used delay times τ ranging from $0.01T_0$ to T_0
 149 with a step size of $0.01T_0$, where $T_0 = 1/f$ is the fundamental period of the signal, and
 150 embedding dimensions m range from 3 to 9. Since one point cannot create any vectors,
 151 and two points can only construct a vector with two possible directions, up and down,
 152 $m = 3$ becomes the smallest embedding dimension to assemble ordinal patterns (Zanin
 153 et al., 2012). In this test, $m = 9$ was chosen as the upper limit due to the high com-
 154 putational cost. To find out whether the wavelength of the targeted signal should be con-
 155 sidered when choosing the window length, we tested 8 different monochromatic signals
 156 with different wavelengths. All synthetic tests were performed using Python (Van Rossum
 157 & Drake, 2009).

158 We first tested a pure monochromatic signal with $f = 1$ Hz (Fig. 2a) to evalu-
 159 ate the effect of different delay times and embedding dimensions. We observed that the
 160 minimum PE is obtained when the shortest delay time, i.e. $\tau = 0.01$ s, and a delay time
 161 τ close to T_0 was used (Fig. 2c). We expected that the minimum PE is obtained when
 162 using $\tau = T_0$, since the delay time will select equal values of amplitude and construct
 163 a repeated ordinal pattern through the window. However, we obtained a very high PE,
 164 close to 1 (Fig. 2c). After checking the synthetic sine wave constructed using the numpy
 165 library (Harris et al., 2020), we found that there are small differences in the order of $10^{(-16)}$
 166 between the amplitudes of the same wave phase, due to the floating error. While the rel-
 167 ative differences between values are negligible, the tiny differences disturb the ranking
 168 and create random ordinal patterns, resulting in PE close to 1.

169 To make the time series more complex, in the next step, we (i) added noise to the
 170 signal and (ii) added different frequencies to create different signal types. We quantified
 171 the noise level by the signal-to-noise ratio (SNR), defined as the ratio between the vari-

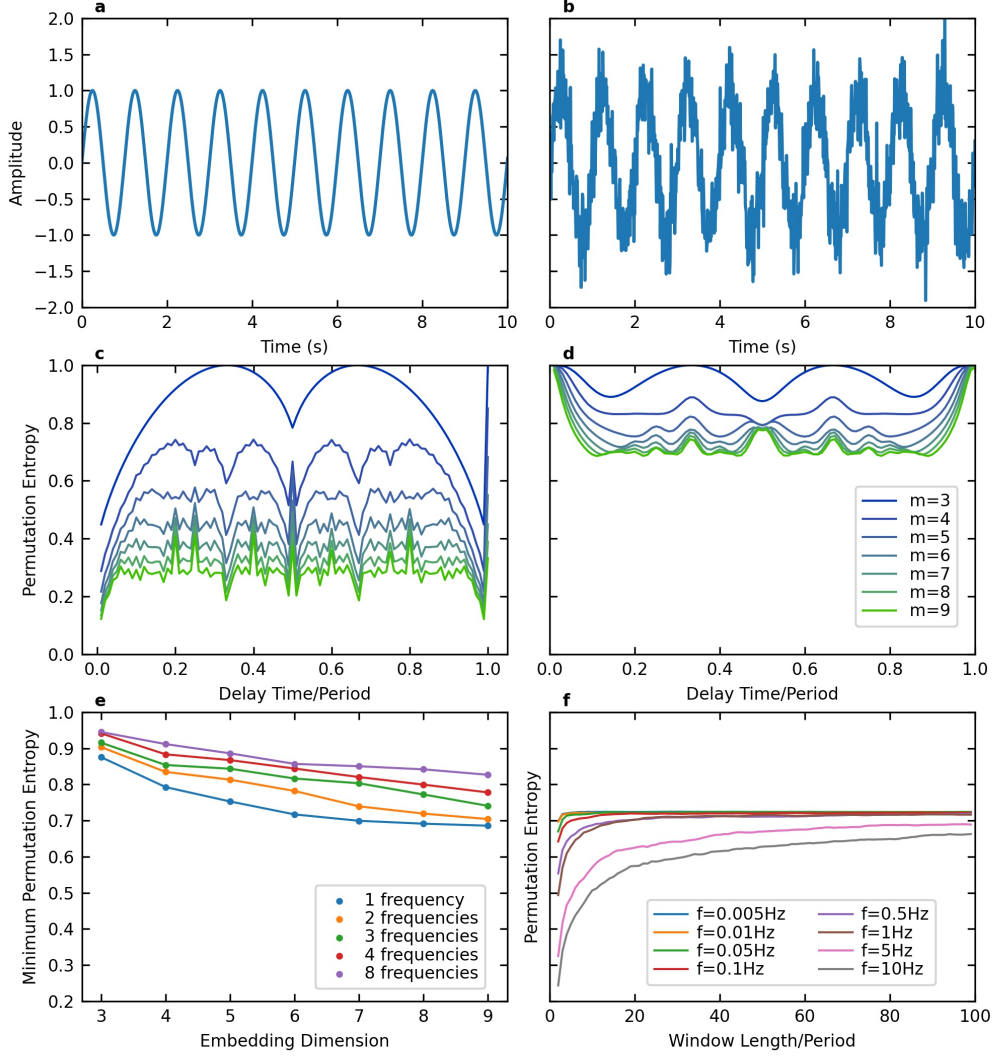


Figure 2. Synthetic test for PE calculation. 10 s zoom of the 2000 s synthetic signal with a frequency of $f=1$ Hz (a) without noise, (b) with $SNR=5$, (c) PE calculated from the signal in subfigure (a) using embedding dimensions m from 3 to 9 and delay times τ from $0.01 T_0$ to T_0 with step size $0.01 T_0$. $T_0=1/f$ is the period of the signal. (d) Same as subfigure (c) for the signal in subfigure (b), (e) Minimum PE values for 5 synthetic signals, with different complexity and $SNR=5$, calculated using the same embedding dimensions and delay times as in subfigure (c), (f) PE calculated for 8 different monochromatic signals with frequencies f between 0.005 and 10 Hz using $m=7$ and $\tau=0.2/f$. The synthetic signals used for subfigures (e) and (f) are shown in Fig. S1.

172 ance of signal and noise. The SNR hence can be calculated according to

$$SNR = \frac{\sigma_S^2}{\sigma_N^2} \quad (2)$$

173 where σ_S is the standard deviation of the signal and σ_N is the standard deviation of the
 174 noise. We used $SNR=5$ to create noise and added it to the monochromatic signal (Fig. 2b).

175 The analysis of the synthetic signal shows that PE is equal to 1 when calculated using
 176 the shortest delay time and delay time equal to T_0 (Fig. 2d). We infer that the delay time
 177 should be short when the signal has a high signal-to-noise ratio. However, if the signal
 178 contains noise, the delay time should not be short nor equal to the fundamental period.

179 In the next step, we generated four different signals containing two, three, four, and
 180 eight frequencies, with and without noise (see Fig. S1 for the detailed information on the
 181 frequency content). The PE was calculated using the same delay time and embedding
 182 dimension as for the monochromatic signal. The result shows higher PE obtained for the
 183 signal containing more frequencies (Fig. 2e and Fig. S1). Similar to the monochromatic
 184 signal without noise, the minimum PE is obtained using $\tau = 0.001 s$ and τ close to T_0 .
 185 While the signals with noise reach PE close to 1 when using $\tau = 0.001 s$ and τ close
 186 to T_0 .

187 According to the PE result in Fig. 2c and d, and Fig. S1, using a higher embed-
 188 ding dimension will result in a lower PE. To see how the PE changes, we plotted the min-
 189 imum PE for the monochromatic signal (Fig. 2b) and four different signals in Fig. S1 with
 190 SNR=5 in Fig. 2e. The minimum PE is obtained for each embedding dimension, calcu-
 191 lated from different delay times ranging from $0.01T_0$ to T_0 . PE generally converges for
 192 each signal, meaning that PE decreases less when using higher embedding dimensions.

193 Another requirement for PE calculation is that the window length has to accom-
 194 modate the maximum number of possible ordinal patterns. Additionally, we need to con-
 195 sider the dominant period of the targeted signal. We tested eight different monochro-
 196 matic signals, with the frequencies f ranging from 0.005 Hz to 10 Hz (see Fig. 2d for the
 197 detailed list of frequencies) with SNR=5 and a sampling frequency of 100 Hz. PE was
 198 calculated using $m = 7$ and $\tau = 0.2T_0$ (see Fig. 2d). The delay time $\tau = 0.2T_0$ was
 199 chosen based on the result in Fig. 2f, where PE is minimum using $\tau = 0.2T_0$. The max-
 200 imum possible number of different ordinal patterns related to the embedding dimension
 201 of 7 is 7! or 5040 ordinal patterns. The PE calculated for the signals with low frequen-
 202 cies, e.g. 0.005 Hz and 0.01 Hz, are stable when the window length is $3 T_0$. In this case,
 203 the signal is much longer than required by $m = 7$. However, the number of points within
 204 $3 T_0$ reduces with increasing signal frequencies given the fixed sampling frequency. There-
 205 fore, the signals with frequencies higher than 1 Hz require more than $3 T_0$ to accommo-
 206 date the points required by the embedding dimension. In conclusion, the window length
 207 should provide enough points for the embedding dimension and be longer than the tar-
 208 geted signal period.

209 2.3 Receiver Operating Characteristic (ROC) Analysis

210 A well-known method to analyze the ability to predict an event, such as earthquakes
 211 or volcanic eruptions (DeVries et al., 2018; Spampinato et al., 2019), is the receiver op-
 212 erating characteristic (ROC) analysis (Fawcett, 2006). ROC analyzes the value of the
 213 predictor variable relative to a threshold. Four possible outcomes are possible: If the vari-
 214 able exceeds the threshold and an event (i.e., eruption in our case) follows within the alarm
 215 period (the subsequent N_T time steps), it is a hit (true positive, TP); otherwise, it is a
 216 false alarm (false positive, FP). If no alarm is raised because the variable is below the
 217 threshold, either no event might occur (true negative, TN), or an event occurs (false neg-
 218 ative, FN) within the next N_T time steps. In this way, each value of the time series is
 219 associated with one of the values TP, FP, TN, or FN, and their counts are calculated
 220 for the whole time series. Based on these counts, the true positive rate $TPR = TP / (TP$
 221 $+ FN)$ and the false positive rate $FPR = FP / (TN + FP)$ are determined. The ROC
 222 curve is finally created by plotting TPR against FPR for threshold values ranging from
 223 the minimum to the maximum value of the assessed variable (here, RMS or PE). Both
 224 TPR and FPR range between 0 and 1. For quantification, the area under the TPR curve
 225 (AUC) is calculated for FPR ranging from 0 to 1. An optimal predictor variable has $AUC=1$,

226 while the ROC curve of a random variable scatters around the diagonal with $AUC \approx 0.5$.
 227 We applied this method to our PE and RMS time series, using a time window of 1 s to
 228 predict an eruption in the following 1 s window.

229 **3 Overview of Instrument Network near Strokkur and Eruption Be-** 230 **haviour of Strokkur**

231 Strokkur geyser is a part of the Geysir geothermal area in the Haukadalur valley
 232 in southwest Iceland (Fig. 1). On the surface, Strokkur hosts a water-filled pool of 12 m
 233 in diameter (Rinehart, 1986). In the middle of the pool, the uppermost part of the sin-
 234 ter conduit walls extends to the surface (Eibl et al., 2021). This conduit is 2.2 m wide
 235 and changes shape and width with depth (Walter et al., 2020). Strokkur features sin-
 236 gle to sextuple eruptions with one to six water fountains jetting into the air with an av-
 237 erage interval of 16.1 s between fountains (Eibl, Hainzl, et al., 2020). Within this manuscript,
 238 we only assessed single to quadruple eruptions for which the waiting time after eruptions
 239 increases linearly from 3.7 ± 0.9 minutes to 11.3 ± 2.9 minutes (Eibl, Hainzl, et al., 2020).

240 We used seismic data recorded at 5 to 14 m distance south and east of the pool of
 241 Strokkur geyser, Iceland (Eibl, Walter, et al., 2020). The sensors are Nanometrics Tril-
 242 lium Compact Posthole 20 s seismometers at locations S2, S3, S5 and Nanometrics Tril-
 243 lium Compact 120 s at locations S1, S4 (see Fig. 1b) in the 7L seismic network (Eibl,
 244 Walter, et al., 2020). The seismometers were installed on 10 June 2018 for 4.5 to 5.25
 245 hours and recorded at a sampling rate of 400 Hz. To assess the sensitivity of PE with
 246 respect to station distance from the source, we utilized the seismic data recorded at sta-
 247 tions G2, G3, and G4 at a distance of 42.5 m, 47.3 m, and 38.3 m. For the latter stations,
 248 no data is available from 10 June, which does not hinder a comparison since the erup-
 249 tive pattern does not change with time (Eibl, Müller, et al., 2020). The data used are
 250 recorded on 3 June 2018 using a sampling rate of 200 Hz.

251 Based on the same seismic dataset, Eibl et al. (2021) suggested that the conduit
 252 is linked to a horizontal crack and a bubble reservoir at 23.7 ± 4.4 m depth, where the
 253 bubble reservoir extends from about 13 to 23 m west of the conduit and feeds eruptions
 254 of Strokkur. Strokkur passes through 4 phases during an eruptive cycle as laid out by
 255 Eibl et al. (2021) based on a multidisciplinary experiment (Eibl, Müller, et al., 2020).

256 The eruptive cycle at Strokkur starts with Phase 1 (P1), when an eruption is con-
 257 firmed visually: a rising bubble slug reaches the surface, bursts, and pushes the water
 258 and steam upwards into a jetting water fountain. P1 ends when the eruption stops. Due
 259 to the water loss in the conduit, the water from the pool and water from a shallow aquifer
 260 flow back to refill the conduit. This process is identified as Phase 2 (P2). At the begin-
 261 ning of Phase 3 (P3), the water temperature in the bubble reservoir is low due to the
 262 heat loss during the eruption. Seismically, this phase features an eruption coda inter-
 263 preted as steam entering the reservoir, which partly collapses (Eibl et al., 2021). The col-
 264 lapses release heat and therefore increase the temperature of the water in the bubble reser-
 265 voir, eventually supporting the gas accumulation toward the end of P3. In Phase 4 (P4),
 266 bubbles regularly leave the bubble reservoir, migrate through the horizontal crack, and
 267 collapse at a temporal spacing of 21 to 26 s when reaching the water in the conduit that
 268 is not hot enough to preserve the steam bubble. With the water in the conduit heating
 269 up, the system eventually reaches conditions where steam bubbles burst on the surface,
 270 and the next eruption starts (P1).

271 **4 Seismic Preprocessing and PE Setting at Strokkur**

272 Previous volcano-seismic studies (Glynn & Konstantinou, 2016; Melchor et al., 2020)
 273 used only the vertical component of seismic data to calculate PE. We compared PE us-
 274 ing the vertical and both horizontal components (Fig. S2) of the stations S1, S2, S3, S4,
 275 and S5. While the PE trends of the three components are generally the same, the ver-

276 tical component exhibits larger variations in PE. We also checked and compared the seis-
 277 mogram and the spectrogram of the three components. The vertical components of these
 278 5 stations display the largest amplitude. Therefore, we used the vertical components for
 279 the following analysis. Station G3 and G4 recorded larger amplitudes on the horizon-
 280 tal components while G2 on the vertical component. The seismic data were detrended,
 281 tapered, and instrument corrected to velocity. Afterward, a high pass Butterworth fil-
 282 ter of order 4 with a corner frequency of 1 Hz was applied to remove the oceanic micro-
 283 seism.

284 Based on the eruption catalog compiled by Eibl et al. (2019), there were 63 erup-
 285 tions recorded on 10 June 2018 from midnight to 04:17 in the morning. These eruptions
 286 consisted of 53 single eruptions, 8 double eruptions, one triple eruption, and one quadru-
 287 ple eruption. As the waiting times after eruptions are in the order of minutes, and changes
 288 within the cycle occur within less than a second (Eibl et al., 2021), we aim for PE with
 289 high temporal resolution. In that case, we need to find the shortest window length poss-
 290 sible to calculate PE. We chose a window length of 1 s as it provides a good temporal
 291 resolution. The window length needs to contain more samples than the maximum poss-
 292 ible $m!$ ordinal patterns constructed from the embedding dimension m . In this case, the
 293 highest embedding dimension that can be applied for a 1 s window length with a sam-
 294 pling frequency of 400 Hz is 5.

295 Since the stations are a few meters from the place where the bubbles burst (Fig. 1),
 296 the signal-to-noise ratio is high. According to our synthetic test of signals without noise
 297 in Fig. 2a, the minimum PE is obtained using the shortest delay time. To confirm this
 298 in the real seismic data, we compare five different estimations using small delay times,
 299 ranging from 0.0025 s to 0.0125 s (Fig. S3). The PE variations related to these five dif-
 300 ferent delay times exhibit consistent patterns, with a difference in the absolute values.
 301 As we are only interested in relative PE changes during the eruptive cycle and not in its
 302 absolute values, it is safe to use one of them. In this paper, we present the result of PE
 303 using a delay time of 0.005 s.

304 In addition to PE, we calculated the Root-Mean-Square (RMS) of the ground mo-
 305 tion in velocity using the same 1 s long time window. Both quantities will be further eval-
 306 uated for their performance in eruption forecasting.

307 5 Results

308 5.1 PE and RMS Variation during an Eruptive Cycle

309 Repetitive patterns of the eruptive cycle for 63 eruptions recorded on 10 June 2018
 310 are visible in seismogram, spectrogram, RMS, and PE. An exemplary single eruption start-
 311 ing at 00:24:39 recorded at station S1 is shown in Fig. 3a-d.

312 The RMS rises at the beginning of P1 and drops at the end of P1 (Fig. 3c). It stays
 313 low during P2 but increases again when P3 starts. In P3, RMS shows a so-called erup-
 314 tion coda composed of seismic peaks at a temporal spacing of 1.5 to 1.7 s featuring a fast
 315 increase and a slow decrease in amplitude. The RMS features regular peaks during P4
 316 at an average temporal spacing of 22 to 27 s. Each of these peaks is followed by a weak
 317 eruption coda, while the seismic amplitude of the peaks tends to decrease towards the
 318 end of P4 (Eibl et al., 2021). The last peak is not followed by an eruption coda.

319 Fig. 3d exhibits a high PE of 0.89 at the beginning of P1, then increases to the max-
 320 imum value at 0.94. PE slightly decreases at the start of P2 and suddenly drops towards
 321 P3. In P3, PE reaches a minimum value of 0.57, followed by a gradual increase towards
 322 P4. At the start of P4, PE reaches a value of 0.81 and sharply drops to 0.60. The fol-
 323 lowing trend then repeats several times: The PE gradually increases to about 0.83 and
 324 sharply decreases to about 0.61. In the last 12 s of P4, PE reaches a value of 0.80 and

325
326

remains high before it increases further and the next eruption (P1) starts. The double, triple, and quadruple eruptions also show similar patterns.

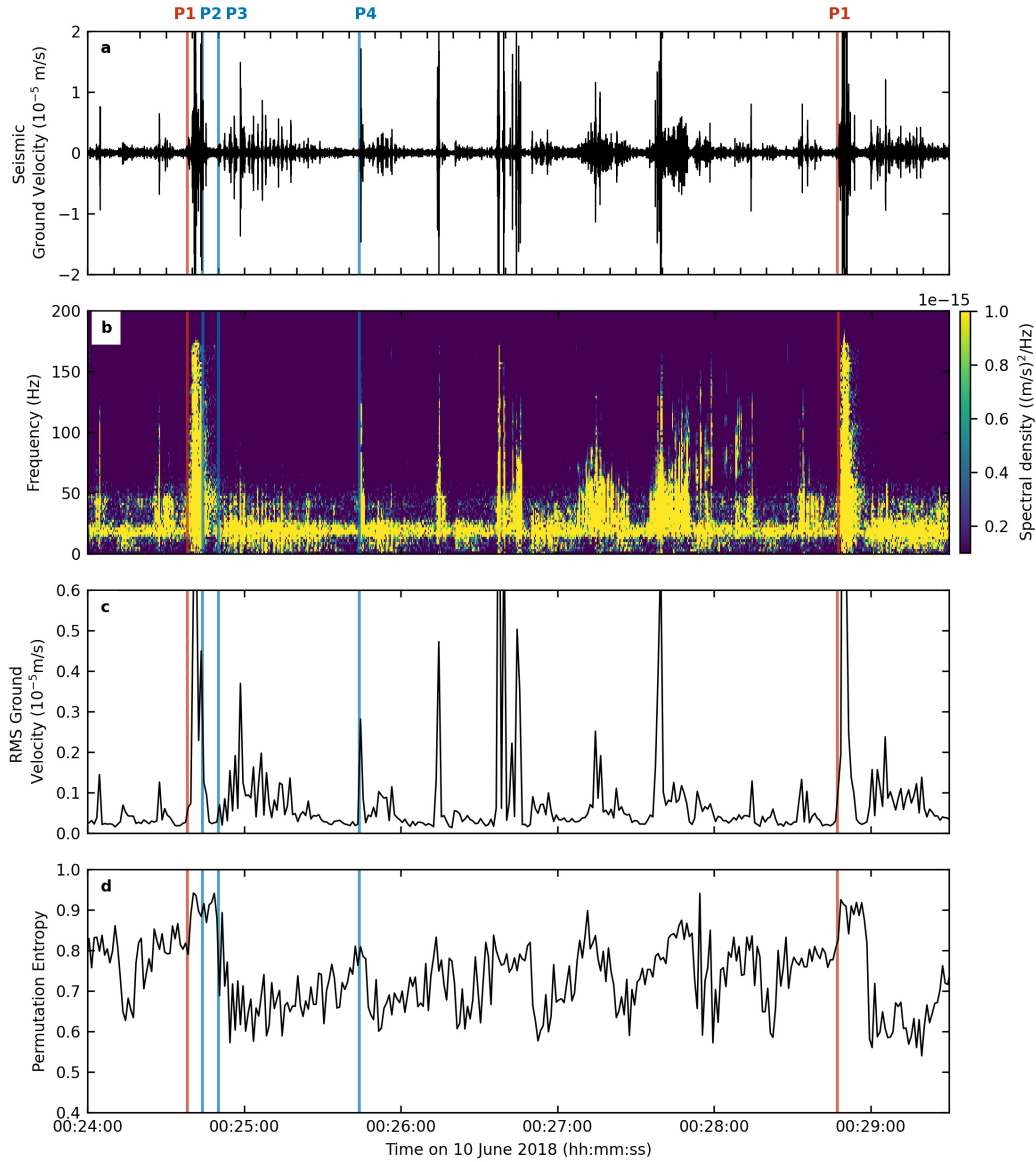


Figure 3. A typical eruptive cycle of a single eruption at 00:24:38 on 10 June 2018. (a) Seismogram of the vertical component after high pass filtering with a corner frequency of 1 Hz. The vertical red line indicates the start of P1, while the blue lines indicate the start of P2, P3, and P4 according to Eibl et al. (2021). (b) Amplitude Spectrogram of subfigure (a) using a time window of 256 samples and overlap of 50 samples. (c) RMS and (d) PE calculated in non-overlapping 1 s long time windows for the seismic data shown in subfigure (a).

327
328

5.2 Stacked PE, RMS, and Hypocentral Distances of 53 Single Eruptions

329
330
331
332
333
334
335

To assess the repetitive pattern of PE and RMS, we stacked the PE and RMS of the 53 cycles, started with a single eruption, according to the start time of each phase. For better visualization, we calculated the mean and the 68% confidence interval (written as mean [lower bound, upper bound]) using a 1 s window. The 68% confidence interval is equivalent to plus/minus one standard deviation for a Gaussian distribution. If the pattern of PE and RMS in each phase is similar from one eruption to another eruption, stacking them will reduce the noise and enhance the pattern.

336
337
338
339
340
341
342
343
344
345

We aligned the RMS from 55 s before to 50 s after the onset of each phase (Fig. 4a-d). The stacked RMS on each phase shows a clear pattern. At 35 s and 15 s before the onset of P1, two seismic peaks reach the mean RMS of $8.2 \cdot 10^{-7}$ m/s and $9.4 \cdot 10^{-7}$ m/s, respectively. While both peaks are followed by a decrease in seismic amplitude, the second last peak is also followed by a weak eruption coda (Fig. 4a). At the onset of P1, the seismic amplitude increases toward the peak at the mean velocity of $7.9 [3.4, 11] \cdot 10^{-6}$ m/s (Fig. 4a). It drops rapidly to the onset of P2 (Fig. 4b). At the onset of P3, the seismic amplitude increases fast to the mean velocity of $1.2 [0.5, 1.9] \cdot 10^{-6}$ m/s and slowly decreases towards the end of the phase (Fig. 4c). P4 starts with a sudden peak of mean velocity with a value of $6.7 [3.8, 9.9] \cdot 10^{-6}$ m/s followed by a weak eruption coda (Fig. 4d).

346
347
348
349
350
351
352
353
354
355
356
357

The stacked PE shows a stable pattern during the different eruptive cycles with different behavior than RMS. Around 35 s before the eruption, we see the last peak reaching a value of 0.78 [0.72, 0.83] in P4. Then the PE value drops to 0.68 [0.59, 0.76] about 27 s before the eruption. Around 15 s before the eruption, the mean of PE reaches a similar value as the last peak of P4. However, instead of decreasing like after the previous peaks, PE remains high for about 6 s and then increases for 8 s to 0.90 [0.88, 0.93] at the start of P1 (Fig. 4e). The PE decreases slightly to P2 and drops to 0.70 [0.61, 0.78] at the beginning of P3 (Fig. 4f-g). PE continues declining for around 3 s to the minimum PE of 0.63 [0.57, 0.68]. After reaching the minimum, PE increases gradually for about 31 s to 0.80 [0.77, 0.82] at the onset of P4 (Fig. 4h). PE then rapidly decreases to 0.63 [0.59, 0.80] for about 8 s after the peak. This pattern repeats several times in P4 before the pattern changes about 14 s before P1.

358
359
360
361
362
363
364
365
366
367
368
369

To investigate the relation between PE and the distance to the source, we calculated the distances from the estimated median source locations (Eibl et al., 2021) to the station S1. S1 is located about 10 m to the south of the conduit on the surface. Eibl et al. (2021) estimated the source location by using the particle motion of the recorded seismic waves. The epicenters of the sources were estimated from the intersection of the azimuth angles derived from all 5 stations. Eibl et al. (2021) project the epicenter location vertically down and extract the source depth from the intersection point with the derived incidence angles for all stations. Note that the shallow source depths during P1 and peaks in P4 are poorly constrained since the particle motion shows an elliptical particle motion characteristic for Rayleigh waves when the seismic sources reach or approach the surface. We stacked the hypocentral distances from the sources to S1 and calculated their mean and the confidence interval (Fig. 4i-l).

370
371
372
373
374
375
376
377
378

We notice that from 15 s before the eruption, the seismic sources remain at about 10 m depth from the surface or about 20 m away from S1 until the eruption occurs (Fig. 4i). The source gradually deepens in P2 and reaches a distance of 34 m from S1 (Fig. 4j-k). The sources in P3 are mostly located 13 to 23 m west of the conduit (Eibl et al., 2021), then hypocentral distances decrease toward P4. We checked the source depth and observed that the seismic sources migrate upwards. P4 starts with seismic sources at a depth of about 10 m with a distance of 21 m to S1. It is likely that the seismic source reached shallower depths during the peaks in P4 (Fig. 4l) and even more during P1, when the eruption occurs on the surface (Fig. 4i).

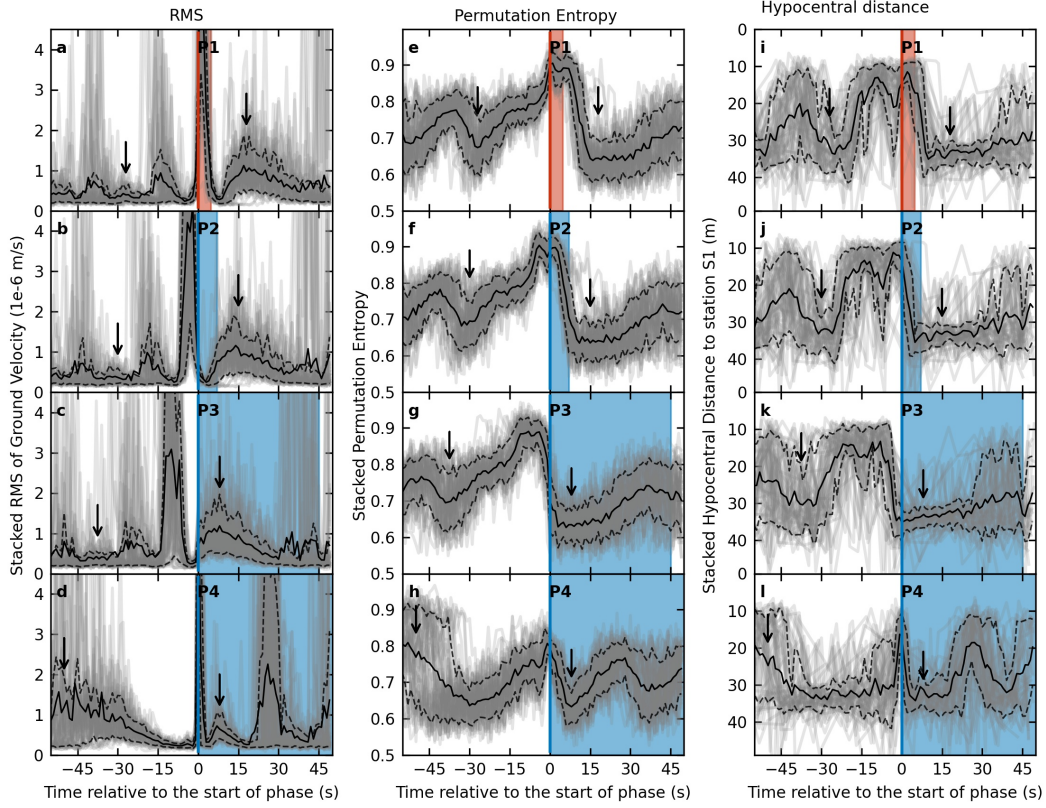


Figure 4. Stacked RMS, PE, and hypocentral distance values for the 53 cycles of single eruptions recorded at station S1. Grey lines mark the RMS values for each eruption aligned at (a) the start of the eruption (P1), (b) the end of the eruption (start of P2), (c) the start of the eruption coda (P3), and (d) the start of P4 with regular bubble collapses in the conduit at depth. The time is measured relative to the alignment time (i.e., the start of the red or blue area highlighting the mean duration of the phase). The black lines define the mean values in a 1 s window, while the dashed lines represent the 68% confidence interval. The black arrows point to the seismic eruption coda visible in P3 and P4. (e-l) Same as subfigures (a-d) for (e-h) PE and (i-l) the distance between the seismic source location and station S1 (Eibl et al., 2021).

379

5.3 PE Pattern with Respect to Double to Quadruple Eruptions

380

381

382

383

384

385

386

387

388

We also assessed the PE pattern of 8 double eruptions recorded on 10 June 2018. These eruptions consist of two water fountains at an average temporal spacing of 15.6 s, and the duration of phases P3 and P4 increase linearly with respect to single eruptions (Eibl et al., 2021). The PE pattern of double eruptions throughout the cycle is similar to single eruptions. Its variation is not systematically higher or lower than for single eruptions. While in single eruptions, the PE drastically drops, on average, after 8 s from the beginning of the eruptions, the PE of double eruptions remains high until the second water fountain. PE only drops when entering P3 on average 28 s after the beginning of the first water fountain (Fig. S4).

389

390

There was only one triple and one quadruple eruption during the whole recording period. In general, the PE patterns for both triple and quadruple are similar to the sin-

391 gle and double eruptions, with PE remaining high in P1 until the last water fountain oc-
 392 curred.

393 **5.4 Reliability of PE Results with Respect to Distance from the Source**

394 To evaluate the performance of PE with respect to the station location, we com-
 395 pared the stacked PE variations obtained for the records at stations S1, S2, S3, S4, and
 396 S5. We also calculated the variations of the stacked source-station distance for the same
 397 stations in the same way. Supplementary Fig. S5 shows that PE is sensitive with respect
 398 to the stations location. The differences in source distance to each station are small, but
 399 the absolute values of PE for different stations are quite distinct. S1, which is located
 400 closest to the seismic sources, exhibits the lowest absolute values of PE compared to the
 401 other stations. S2, S3, and S4 display a similar temporal variation as S1 but with higher
 402 absolute values throughout the cycles. An exception is station S5. While the distance
 403 from S5 to the seismic sources is similar to the other stations, the temporal variation of
 404 PE does not reflect clearly the changing phases in the eruptive cycle. Overall, the PE
 405 at station S5 is dominated by high values except for the first half of P3. The PE in P4
 406 is as high as in P1, making it difficult to see the transition to the eruption in the PE value.

407 To investigate further the performance of PE at stations with a larger distance, we
 408 calculated PE of seismic data recorded at stations G2, G3, and G4 (Fig. 1b) on 3 June
 409 2018. These three stations are located at 42.5 m, 47.3 m, and 38.3 m north-west, west,
 410 and south-east of the conduit, respectively. However, the temporal variation of PE on
 411 these stations does not correlate with the phases in the eruptive cycle.

412 **6 Interpretation and Discussion**

413 **6.1 The relation between PE and Strokkur eruptive cycle**

414 PE does not depend on the absolute amplitudes, and multiplying a signal by a fac-
 415 tor leads to the same PE value. In contrast, PE depends on the frequency bandwidth
 416 of the signal. Our synthetic test shows that a synthetic signal containing more frequen-
 417 cies, i.e., by superposing more harmonic signals, produces a higher PE than a signal con-
 418 taining fewer frequencies. We suggest that a signal with a broader frequency content has
 419 a higher PE compared to a signal with a narrower frequency band. Dávalos et al. (2021)
 420 investigated the effect of bandpass filters such as Butterworth and Chebyshev applied
 421 before the PE calculation and observed that lower PE corresponded to narrower band-
 422 widths while higher PE corresponded to broader bandwidths. Our synthetic tests con-
 423 firm their result.

424 Our observation at Strokkur shows that PE reaches the highest value during the
 425 eruption phase (P1) when the water jets into the air. In this phase, the amplitude peaks
 426 and the frequency content is broad. Once the last fountain stops (P2), the amplitude quickly
 427 drops and declines to narrower bandwidth. PE is still high at the end of the last foun-
 428 tain but then quickly drops to the next phase (P3). During P3, the eruption coda is com-
 429 posed of seismic peaks at a temporal spacing of 1.5 to 1.7 s. Whilst their frequency con-
 430 tent is broad, it is not as broad as during seismic peaks in P1 and P4. Between these
 431 peaks in P3, the frequency content of the seismic signal is narrow banded, and the PE
 432 fluctuates and reaches minimum values. In P4, during the regular peaks and broad spec-
 433 trum of the energy produced by the bubble collapses at depth, PE reaches the local max-
 434 imum. Conversely, PE is smallest directly after the peaks in P4 despite a starting erup-
 435 tion coda that increases in amplitude and widens in frequency content. Shortly before
 436 the next peak in P4, it seems seismically quiet and with a narrow-banded frequency con-
 437 tent while the PE value keeps increasing. The PE hence does not solely depend on the
 438 broadness of the frequency spectrum.

439 During P4, the two last bubble collapses at depth in the conduit happen about 35
 440 and 15 s before the start of the next eruption, respectively. Both collapses are recorded
 441 as a peak in seismic amplitude and are followed by a drop in seismic amplitude, as seen
 442 in the stacked RMS. During these collapses, the PE values reach a local maximum. Fol-
 443 lowing the second last collapse, the PE value drops, while it remains high after the last
 444 bubble collapse. We further investigated the waveforms and spectrograms in the last 50 s
 445 before the eruption. The second last collapse is followed by a weak eruption coda. This
 446 coda is similar to the eruption coda in P3 in terms of the peaks' temporal spacing and
 447 frequency content. However, it is smaller in amplitude, and the duration is shorter than
 448 in P3. In contrast, the last collapse before the eruption is not followed by an eruption
 449 coda. Hence, the RMS value drops to a lower amplitude while the PE value remains high.
 450 With respect to the state of the geyser, this implies that the second last bubble collapse
 451 triggers recharge in the reservoir, while after the last bubble collapse at depth, the sys-
 452 tem has reached a state that is ready for eruption. At that stage, the water in the reser-
 453 voir and conduit is most likely heated sufficiently - without further need to recharge -
 454 and contains small bubbles in the whole pipe system. The next large bubble that rises
 455 in the conduit can then reach the surface and burst into a jetting water fountain.

456 Eibl et al. (2021) observed a decrease in seismic peak amplitude during collapses
 457 in the conduit with time. They speculate that this is due to damping when more bub-
 458 bles accumulate in the conduit and decouple the noise from the bubbles and the conduit
 459 walls. Here, an increasing amount of bubbles might then suggest that the PE values through-
 460 out P4 should increase. While in some eruptions, such an increase can be observed through-
 461 out P4, it is not always the case. Glynn and Konstantinou (2016) observed an increase
 462 of PE for two days between a 5.6 Mw earthquake in Bárarbunga on 29 September 1996
 463 and the onset of a subglacial eruption in Gjalp on 1 October 1996. This PE increase was
 464 preceded by 8 days of PE decrease, which they associated with the lack of frequency higher
 465 than 1 Hz. After the 5.6 Mw earthquake, earthquake swarms migrated to the Gjalp fis-
 466 sures featuring a broader frequency content up to 7 Hz (Konstantinou et al., 2000). Glynn
 467 and Konstantinou (2016) suggested that these higher frequencies increase the complex-
 468 ity, hence causing the PE increase.

469 6.2 How the station distance could affect the PE value

470 We observed that the PE at stations S1, S2, S3, and S4 correlates strongly with
 471 the distance between seismic sources and the station. As the seismic sources migrate to
 472 the surface and the source-station distance decreases, PE increases. We suspect that the
 473 attenuation during the seismic wave propagation could play a role. When the source is
 474 at a larger depth, the seismic wave travels a longer path, and more of the higher frequen-
 475 cies are attenuated and scattered. As a result, the PE value of this signal should be low.
 476 As the source moves closer to the surface, the seismic wave travels a shorter distance and
 477 attenuates less, yielding a higher PE value. This observation is similar to Glynn and Kon-
 478 stantinou (2016), where the increase of PE due to the earthquake migration prior to the
 479 1996 Gjalp eruption is smaller at the further stations. Glynn and Konstantinou (2016)
 480 also suggested that this due to the attenuation. However, the attenuation cannot be the
 481 only reason, as S5 has, on average, a larger distance to the sources compared to S1-S4
 482 but shows larger PE values with a different pattern than the other four stations. Eibl
 483 et al. (2021) observed that stations S1 to S4 exhibit high linearity in the particle mo-
 484 tion from the deep seismic source, while station S5 exhibits significantly lower linearity
 485 and was hence excluded from the depth location. The lower data quality of S5 may also
 486 cause high PE values at station S5.

487 At larger distance of 38.3 to 47.3 m, PE does not perform well. We observed that
 488 PE at stations G2, G3, and G4 exhibit lower values with no clear precursory signal. Our
 489 synthetic test (Fig. 2) shows that PE is sensitive to the presence of noise. When the dis-
 490 tance of the source to the station is far, and the signal strength in the recorded seismo-

gram is low, PE seems to reflect the dynamics of the local station environment more than the eruptive cycle of the Strokkur geyser. This is also supported by findings of Eibl et al. (2021) who could not use these stations for the seismic source location due to low-quality particle motions.

6.3 Predictive power of PE in comparison to RMS

We used the ROC analysis to quantify the predictive power of PE in comparison to RMS. The resulting curves are shown in Fig. 5 for alarms raised for the next time step when the variables exceed a certain threshold. PE demonstrates good predictive skills with $AUC=0.846$, while RMS is even worse than random with $AUC=0.433$. The latter is not surprising, having in mind that RMS tends to decrease prior to eruptions (see Fig. 4e). Thus, we also calculated the inverse of RMS as a measure of quiescence. However, $1/RMS$ yields $AUC=0.567$ which is only slightly better than a random forecast.

To rank the predictive power of the PE using only 1 s bin information, we also applied the statistical recurrence model of Eibl, Hainzl, et al. (2020) which was inferred from 20390 waiting times after eruptions of Strokkur geyser in December 2017 and January 2018. The analysis of this long sequence revealed log-normal recurrences with mean and standard deviations dependent on the eruption type of the last event. In particular, we determined the probability p_T of the next event within the alarm time, knowing the time to the last eruption and its eruption style. This value is found to outperform PE with $AUC=0.971$. Of course, the comparison is unfair because p_T is based on combined information over a very long time. However, PE can even improve the p_T -result if the product of both variables is considered. This result can be understood by considering that p_T is monotonously increasing with increasing time to the last eruption. At the same time, PE is similarly high at intermediate bubble collapses at depth as before the eruptions (see Fig. 3d). The multiplication (shown in the black dashed and continuous lines in Fig. 5) suppresses the high values related to bubble collapses, leading to an enhanced forecast power. This effect is amplified, if the mean ($\langle PE \rangle$) value is removed from the PE signal, $PE_n = (PE - \langle PE \rangle) H(PE - \langle PE \rangle)$, with H the Heaviside function ($H(x)=1$ if $x>0$ and zero else). In this case, the AUC is 0.99, very close to the optimal value of 1.0.

Note that to test the predictive power of PE and RMS, we have only used so far the information in separate 1 s bins of the seismogram. We ignored the information encoded in the time evolution of these parameters. To analyze the possible improvements using the full PE and RMS patterns requires machine learning techniques and is left for future studies.

7 Conclusions

In this research, we show a good capability of PE in characterizing different phases in the eruptive cycle of the Strokkur geyser. PE also performs better in predicting an eruption than RMS of the ground velocity. About 15 s before the eruption, PE indicates that the system is prone to erupt after the last collapse by increasing values. At the same time, the RMS indicates quiescence, and the seismic sources remain at a shallow depth. The PE reflects the seismic changes linked to a status with superheated water in the pipe system and small bubbles drifting in it. Hence, the PE might be indirectly sensitive to the number of small bubbles present in the water.

PE can characterize the different phases of the geyser's eruptive cycle for the near-field stations, but it seems that PE cannot resolve the dynamics for signals at larger distances. Depending on the signal strength at the source and the signal-to-noise ratio, our results indicate that this method requires seismic data recorded as close to the source as possible, in the case of Strokkur within 15 m. Defining suitable preprocessing steps

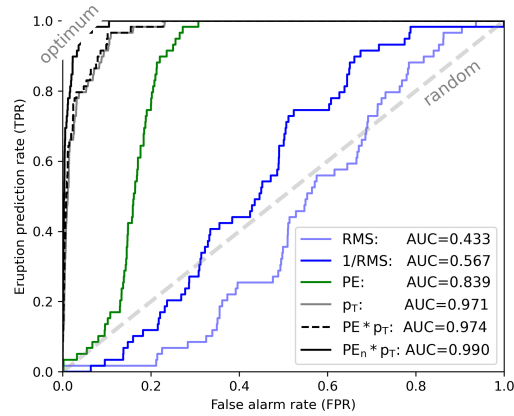


Figure 5. Assessing the predictive power of PE using ROC. ROC curves for PE (green), RMS (light blue), the inverse of RMS (blue), and the probability p_T calculated for the recurrence model of Eibl, Hainzl, et al. (2020) (grey), as well as combinations of the latter with PE (solid black and dashed black). Here, PE_n refers to the rescaled PE value, $PE_n = (PE - \langle PE \rangle) H(PE - \langle PE \rangle)$, with $\langle PE \rangle$ being the mean value of PE and H the Heaviside function. The alarm period is the next time step ($N_T=1$) with the corresponding AUC values given in the legend. The result of a random variable is indicated by the dashed diagonal with AUC=0.5, while the result of an optimal predictor is marked in the upper left corner.

540 for PE application on a volcano requires further research. While in a geyser, the inter-
 541 action between the water and gas with the surrounding rock mostly generates tremors,
 542 the interaction between magma and the surrounding rock in a volcano generates more
 543 types of volcano-seismic signals with different complexities. For monitoring a volcano,
 544 the seismic stations are usually installed at larger distances, which will decrease the sig-
 545 nal strength. These factors need to be taken into account. Nonetheless, PE has a strong
 546 potential to contribute to the framework of eruption forecasting. For this purpose, our
 547 study might help to define distinct precursory features in the temporal variation of PE
 548 prior to eruptions that are useful for eruption forecasting.

549 Acknowledgments

550 We thank the Environment Agency of Iceland and the National Energy Authority for
 551 the research permit around Strokkur in the Geysir geothermal area. We thank the rangers
 552 and Daniel Vollmer for support and guidance in the field. This work was financially sup-
 553 ported by DAAD.

554 We declared that this work does not contain any conflict of interests.

555 References

- 556 Bandt, C., & Pompe, B. (2002). Permutation entropy: A natural complexity
 557 measure for time series. *Physical Review Letters*, 73(17). doi: 10.1103/
 558 PhysRevLett.88.174102
 559 Bell, A. F., Naylor, M., & Main, I. G. (2013, 06). The limits of predictability of
 560 volcanic eruptions from accelerating rates of earthquakes. *Geophysical Journal*
 561 *International*, 194(3), 1541-1553. Retrieved from [https://doi.org/10.1093/
 562 gji/ggt191](https://doi.org/10.1093/gji/ggt191) doi: 10.1093/gji/ggt191
 563 Boué, A., Cortés, G., Vallete, B., & G, R. (2015). Real-time eruption forecasting us-

- 564 ing the material failure forecast method with a bayesian approach. *Journal of*
565 *Geophysical Research: Solid Earth*, 120. doi: 10.1002/2014JB011637
- 566 Dempsey, D. E., Cronin, S. J., Mei, S., & A.W, K. (2020). Automatic pre-
567 cursor recognition and real-time forecasting of sudden explosive volcanic
568 eruptions at whakaari, new zealand. *Nature Communication*, 11. doi:
569 1038/s41467-020-17375-2
- 570 DeVries, P. M. R., Viégas, F., Wattenberg, M., & Meade, B. J. (2018). Deep learn-
571 ing of aftershock patterns following large earthquakes. *Nature*, 560(7720), 632-
572 634.
- 573 Dávalos, A., Jabloun, M., Ravier, P., & Buttelli, O. (2021). The impact of linear
574 filter preprocessing in the interpretation of permutation entropy. *Entropy*, 23.
575 doi: 10.3390/e23070787
- 576 Eibl, E. P. S., Hainzl, S., Vesely, N. I. K., Walter, T. R., Jousset, P., Hersir, G. P., &
577 Dahm, T. (2020). Eruption interval monitoring at Strokkur Geyser, Iceland.
578 *Geophysical Research Letters*, 47, e2019GL085266.
- 579 Eibl, E. P. S., Jousset, P., Dahm, T., Walter, T. R., Hersir, G. P., & Vesely,
580 N. I. K. (2019). Seismic experiment at the strokkur geyser, iceland, allows
581 to derive a catalogue of over 70,000 eruptions. *GFZ Data Services*. doi:
582 <https://doi.org/10.5880/GFZ.2.1.2019.005>
- 583 Eibl, E. P. S., Müller, D., Allahbakhshi, M., Walter, T. R., Jousset, P., Hersir, G. P.,
584 & Dahm, T. (2020). *Multidisciplinary dataset at the strokkur geyser, ice-*
585 *land, allows to study internal processes and to image a bubble trap*. doi:
586 10.5880/GFZ.2.1.2020.007
- 587 Eibl, E. P. S., Müller, D., Walter, T. R., Allahbakhshi, M., Jousset, P., Hersir,
588 G. P., & Dahm, T. (2021). Eruptive cycle and bubble trap of Strokkur
589 Geyser, Iceland. *Journal of Geophysical Research: Solid Earth*, 126. doi:
590 10.1029/2020JB020769
- 591 Eibl, E. P. S., Walter, T., Jousset, P., Dahm, T., Allahbakhshi, D., M.and Müller,
592 & Hersir, G. (2020). 1 year seismological experiment at strokkur in 2017/18.
593 *GFZ Data Services. Other/Seismic Network*. doi: 10.14470/2Y7562610816
- 594 Endo, E. T., & Murray, T. (1991). Real-time seismic amplitude measurement
595 (rsam): a volcano monitoring and prediction tool. *Bulletin of Volcanology*, 53,
596 533-545. doi: 10.1007/BF00298154
- 597 Fawcett, T. (2006). An introduction to ROC analysis. *Pattern Recognition Letters*,
598 27(8), 861-874.
- 599 Glynn, C. C., & Konstantinou, K. I. (2016). Reduction of randomness in seismic
600 noise as a short-term precursor to a volcanic eruption. *Scientific Reports*, 6(1),
601 37733. Retrieved from <http://www.nature.com/articles/srep37733> doi: 10
602 .1038/srep37733
- 603 Harris, C. R., Millman, K. J., van der Walt, S. J., Gommers, R., Virtanen, P., Cour-
604 napeau, D., ... Oliphant, T. E. (2020, September). Array programming with
605 NumPy. *Nature*, 585(7825), 357–362. Retrieved from [https://doi.org/
606 10.1038/s41586-020-2649-2](https://doi.org/10.1038/s41586-020-2649-2) doi: 10.1038/s41586-020-2649-2
- 607 Hurwitz, S., & Manga, M. (2017). The fascinating and complex dynamics of geyser
608 eruptions. *Annual Review of Earth and Planetary Sciences*, 45(1), 31-59. doi:
609 10.1146/annurev-earth-063016-015605
- 610 Konstantinou, K., Nolet, G., Morgan, W., Allen, R., & Pritchard, M. (2000). Seis-
611 mic phenomena associated with the 1996 vatnajökull eruption, central ice-
612 land. *Journal of Volcanology and Geothermal Research*, 102(1), 169-187.
613 Retrieved from [https://www.sciencedirect.com/science/article/pii/
614 S0377027300001876](https://www.sciencedirect.com/science/article/pii/S0377027300001876) doi: [https://doi.org/10.1016/S0377-0273\(00\)00187-6](https://doi.org/10.1016/S0377-0273(00)00187-6)
- 615 McNutt, S. R. (1996). Seismic monitoring and eruption forecasting of volcanoes: A
616 review of the state-of-the-art and case histories. In *Monitoring and mitigation
617 of volcano hazards* (pp. 99–146). Springer Berlin Heidelberg. doi: 10.1007/978
618 -3-642-80087-0_3

- 619 Melchor, I., Almendros, J., Carniel, R., Konstantinou, K. I., Hantusch, M., &
620 Caselli, A. (2020). On data reduction methods for volcanic tremor char-
621 acterization: the 2012 eruption of copahue volcano, southern andes. *Earth,
622 Planets and Space*, 72, 134. doi: 10.1186/s40623-020-01270-7
- 623 Moran, S. C., Freymueller, J. T., LaHusen, R. G., McGee, K. A., Poland, M. P.,
624 Power, J. A., ... White, R. A. (2008). *Instrumentation recommendations for
625 volcano monitoring at u.s. volcanoes under the national volcano early warning
626 system* (Tech. Rep.). U.S. Geological Survey.
- 627 Moran, S. C., Newhall, C., & Roman, D. C. (2011). Failed magmatic eruptions: late-
628 stage cessation of magma ascent. *Bulletin of Volcanology*, 73(2). doi: 10.1007/
629 s00445-010-0444-x
- 630 Riedl, M., Müller, A., & Wessel, N. (2013). Practical considerations of permuta-
631 tion entropy: A tutorial review. *The European Physical Journal Special Top-
632 ics*, 222(2), 249–262. Retrieved from [http://link.springer.com/10.1140/
633 epjst/e2013-01862-7](http://link.springer.com/10.1140/epjst/e2013-01862-7) doi: 10.1140/epjst/e2013-01862-7
- 634 Rinehart, J. S. (1986). Seismic signatures of some icelandic geysers. *Journal of Geo-
635 physical Research*, 73. doi: 10.1029/JB073i014p04609
- 636 Spampinato, S., Langer, H., Messina, A., & Falsaperla, S. (2019). Short-term de-
637 tection of volcanic unrest at Mt. Etna by means of a multi-station warning
638 system. *Scientific Reports*, 9, 6506. doi: 10.1038/s41598-019-42930-3
- 639 Van Rossum, G., & Drake, F. L. (2009). *Python 3 reference manual*. Scotts Valley,
640 CA: CreateSpace.
- 641 Walter, T. R., Jousset, P., Allahbakhshi, M., Witt, T., Gudmundsson, M. T., &
642 Hersir, G. P. (2020). Underwater and drone based photogrammetry reveals
643 structural control at geysir geothermal field in iceland. *Journal of Volcanology
644 and Geothermal Research*, 391. doi: 10.1016/j.jvolgeores.2018.01.010
- 645 White, D. E. (1967). Some principles of geyser activity, mainly from steamboat
646 springs, nevada. *American Journal of Science*, 265(8), 641–684. Retrieved
647 from <https://www.ajsonline.org/content/265/8/641> doi: 10.2475/ajs.265
648 .8.641
- 649 Whitehead, M. G., & Bebbington, M. S. (2021). Method selection in short-term
650 eruption forecasting. *Journal of Volcanology and Geothermal Research*, 419.
651 doi: 10.1016/j.jvolgeores.2021.107386
- 652 Zanin, M., Zunino, L., Rosso, O. A., & David, P. (2012). Permutation entropy
653 and its main biomedical and econophysics applications: A review. *Entropy*, 14,
654 1553-1577. doi: 10.3390/e14081553
- 655 Zunino, L., Olivares, F., Scholkmann, F., & Rosso, O. A. (2017). Permuta-
656 tion entropy based time series analysis: Equalities in the input signal can
657 lead to false conclusions. *Physics Letters A*, 381(22), 1883-1892. doi:
658 10.1016/j.physleta.2017.03.052